ACSNANO

www.acsnano.org

ARTICLE

Efficient Third Harmonic Generation and Nonlinear Subwavelength Imaging at a Higher-Order Anapole Mode in a Single Germanium Nanodisk

Gustavo Grinblat,* Yi Li,* Michael P. Nielsen, Rupert F. Oulton, and Stefan A. Maier

The Blackett Laboratory, Department of Physics, Imperial College London, London SW7 2AZ, United Kingdom

ABSTRACT: Benefiting from large intrinsic nonlinearities, low absorption, and high field enhancement abilities, all-dielectric nanoantennas are considered essential for efficient nonlinear processes at subwavelength volumes. In particular, when the dielectric nanoantenna supports the nonradiating anapole mode, characterized by a minimum in the extinction cross section and a maximum electric energy within the material, third harmonic generation (THG) processes can be greatly enhanced. In this work, we demonstrate that a higher-order anapole mode in a 200 nm thick germanium nanodisk delivers the highest THG efficiency on the nanoscale at optical frequencies. By doubling the diameter of a disk supporting the fundamental anapole mode, we discover the emergence of an anapole mode of higher order, with a valley in the extinction cross section significantly narrower than that of the fundamental anapole. Under this condition, we observe a highly improved electric field confinement effect within the dielectric disk, leading to THG conversion efficiencies as large as 0.001% at a third harmonic wavelength of 550 nm. In addition, by mapping the THG emission across the nanodisk, we are able to unveil the anapole near-field intensity distributions, which show excellent agreement with numerical simulations. Our findings remarkably expand contemporary knowledge on localized modes in dielectric nanosystems, revealing crucial elements for the elaboration of highly efficient frequency upconversion nanodevices.

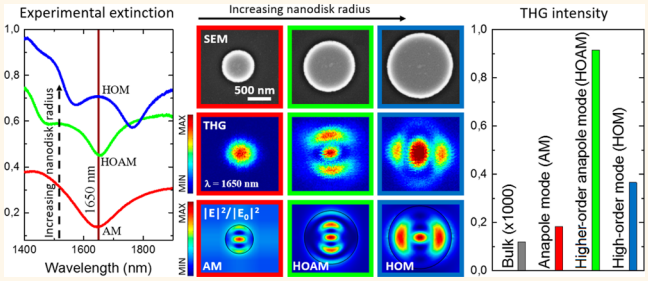

KEYWORDS: *all-dielectric nanodisks, electric field enhancement, anapole modes, third harmonic generation, nonlinear imaging*

Light-frequency upconversion is a phenomenon that converts multiple low-energy photons into one high-energy photon, producing light with higher frequency than the incident radiation. The manipulation of this effect on the nanoscale at the optical regime can benefit a wide variety of existing applications, enhancing (bio)imaging resolution,[1,2] increasing optical sensing sensitivity,[3,4] improving solar light harvesting,[5,6] and bettering control of optically triggered intracellular drug delivery mechanisms.[7,8] Among frequency upconversion processes, third harmonic generation (THG), in particular, is the one that coherently converts three photons of frequency ω into one photon of frequency 3ω.[9−12] In macroscopic crystals, this process can be optimized by fulfilling a phase-matching condition, that is, $n_\omega = n_{3\omega}$ (n is the refractive index), which generates third harmonic (TH) light in phase across the whole excitation volume, leading to a powerful constructive interference effect that maximizes the TH conversion efficiency.[9] However, since this process builds with the interaction length, nanoscale devices, which typically possess characteristic distances that are not even sufficient to incur phase walk-off, are not usually reliant upon engineering a phase-matching condition.

Alternatively, since THG is a third-order effect, with the TH power increasing with the cube of the excitation intensity, the nonlinear performance can also be maximized by locally enhancing the excitation density. One of the most promising approaches exploiting this concept consists of engineering high permittivity materials to produce optical nanoantennas capable of efficiently concentrating light at the fundamental frequency inside them. This strategy not only delivers an effectively increased pump intensity but also, as it utilizes high permittivity materials, provides large intrinsic third-order nonlinear susceptibilities ($\chi^{(3)}$) due to Miller's rule.[13] In this context, nanostructured metals and high refractive index dielectrics are both promising candidates for producing strong nonlinear effects without the need for phase matching due to both field

Received: November 9, 2016
Accepted: December 15, 2016
Published: December 15, 2016

DOI: 10.1021/acsnano.6b07568
ACS Nano 2017, 11, 953−960

confinement and high $\chi^{(3)}$ values.[14−22] However, the conversion efficiency of metallic nanoantennas is severely limited by two effects: first, light is restricted to surface regions, reducing the overlap between the electric field and the nonlinear volume to a minimum; and second, high metallic absorption and associated heat generation limit incident light intensities without nanoantenna degradation.[19,21−23] Extensive research on plasmonic/dielectric/hybrid configurations in recent years[14−17,24−28] has ultimately led to monolithic dielectric nanoantennas as those presenting the greatest performance in terms of nonlinear functionality.[15]

Among standard dielectrics, germanium represents the one that possesses the highest refractive index ($n \sim 4.5$) and, therefore, $\chi^{(3)}$ (>10^{-11} esu) at near-infrared frequencies.[29] At the same time, this material can exhibit up to more than 5 orders of magnitude less linear absorption than metals such as gold in this spectral range.[30,31] Indeed, by producing a 100 nm thick disk-shaped germanium nanoantenna, we have recently reported TH conversion efficiencies as high as 0.0001% at an excitation wavelength of 1650 nm,[15] exceeding the performance of the previously reported silicon nanodisk[14] ($n \sim 3.5$) by nearly an order of magnitude. It is worth mentioning that materials other than germanium have demonstrated comparable efficiencies only through complex arrangements, such as Fano resonant silicon metasurfaces[16] or quadrumers of silicon nanodisks supporting magnetic Fano resonance collective modes.[17]

It is also of high importance, in order to produce large TH conversion efficiencies, in a nanoscale system to understand the resonant modes available to enable their exploitation. For example, in our previously reported case of the 100 nm thick germanium nanodisk,[15] we found that the best nonlinear performance occurred when exciting at the minimum of the extinction cross section described by the anapole mode (AM), at which the electric field confinement within the dielectric is maximum,[15,18] a condition that changes to the magnetic dipole mode when the aspect ratio of the cylinder is sufficiently increased.[14,15] However, while the influence of these and other low-order modes on the nonlinear properties of dielectric nanodisks has been reported,[14,15] the effects of modes of higher order have remained unexplored. Furthermore, while the near-field patterns of the lower-order modes have been theoretically calculated,[14,15,18] experimental characterization attempts through near-field scanning optical microscopy (NSOM) have only poorly revealed actual field distributions.[18]

In this article, by studying individual 200 nm thick germanium nanodisks of different radii, we demonstrate the emergence of a higher-order anapole mode (HOAM) when the disk diameter supporting the fundamental AM is nearly doubled, while keeping the excitation wavelength fixed at 1650 nm. We observe that the linear optical response of the HOAM describes a minimum in the extinction cross section with a valley sharper than that registered at the AM. This characteristic leads to an enhanced field confinement capability that gives rise to a large TH conversion efficiency of 0.001% at an emission wavelength of 550 nm, exceeding the performance of bulk germanium by 4 orders of magnitude and outperforming both the higher- and lower-order modes. In addition, we demonstrate that the profile of the wavelength dependence of the TH intensity matches that of the cube of the simulated electric energy inside the nanoantenna, highlighting the nature of the THG process as a third-order nonlinear volume phenomenon. Finally, by mapping the TH emission across nanodisks of different sizes (schematic in Figure 1), we are able to unveil the electric field intensity distribution corresponding to the different studied modes, showing excellent agreement with numerical calculations.

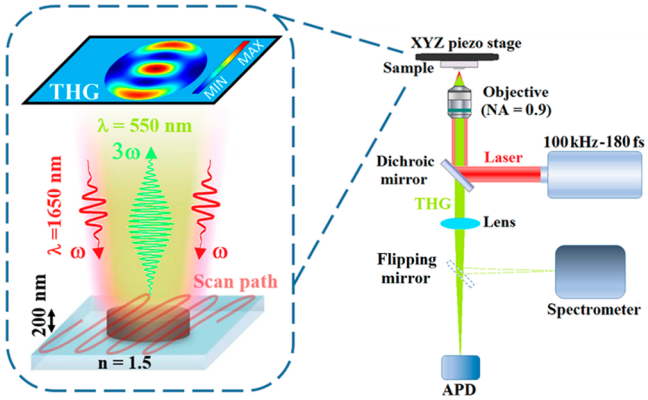

Figure 1. Illustration of the experimental THG mapping setup. A 200 nm thick germanium nanodisk on glass is excited with ultrafast near-infrared light of frequency ω (1650 nm wavelength), and its emission is scanned across the nanostructure in reflection geometry at a frequency of 3ω (550 nm).

RESULTS AND DISCUSSION

Arrays of germanium nanodisks of 200 nm thickness and radius (R) ranging from 300 to 700 nm were produced through electron beam lithography, thermal evaporation, and standard lift-off process (refer to the Methods section for fabrication specifics). A pitch of 4 μm was chosen to avoid optical coupling between adjacent nanostructures. Following fabrication, to determine resonance wavelengths, the extinction cross-section spectra of the nanodisks were characterized through Fourier transform infrared (FTIR) spectroscopy in transmission configuration at normal incidence. At the same time, to theoretically describe the experimental results, we performed corresponding numerical calculations *via* a finite-element method using the commercial software Comsol Multiphysics (further details of the numerical simulations are included in the Methods section).

Figure 2 displays the linear optical response of disks of different sizes, including our previously reported case of the 100 nm thick germanium nanodisk with radius R_{ref} = 440 nm for reference.[15] For the main 200 nm thick nanodisk, three different radii are considered: R_1 = 350 nm, R_2 = 635 nm, and R_3 = 700 nm. In order to account for small deviations of the fabricated structure from the perfect cylinder, we have allowed variations in the radius of around 10% in the numerical calculations to better describe the experimental results. To distinguish from R_1, R_2, and R_3, corresponding values for simulations are denoted as R_1*, R_2*, and R_3*, respectively. The experimental and simulated extinction cross-section spectra of the four studied samples are shown in Figure 2a,b, respectively, showing reasonable agreement in all cases, with maxima and minima occurring at similar wavelengths, correspondingly.

To gain a better understanding of the different modes present in the spectra, we plot, in Figure 2c, the wavelength dependence of the electric energy stored inside the nanodisk, $W_E = n^2 \int\int\int |E|^2 dV/2$, which will be important for our later analysis of the THG process. In particular, at a selected pump wavelength of 1650 nm, we observe that the reference nanodisk

DOI: 10.1021/acsnano.6b07568
ACS Nano 2017, 11, 953−960

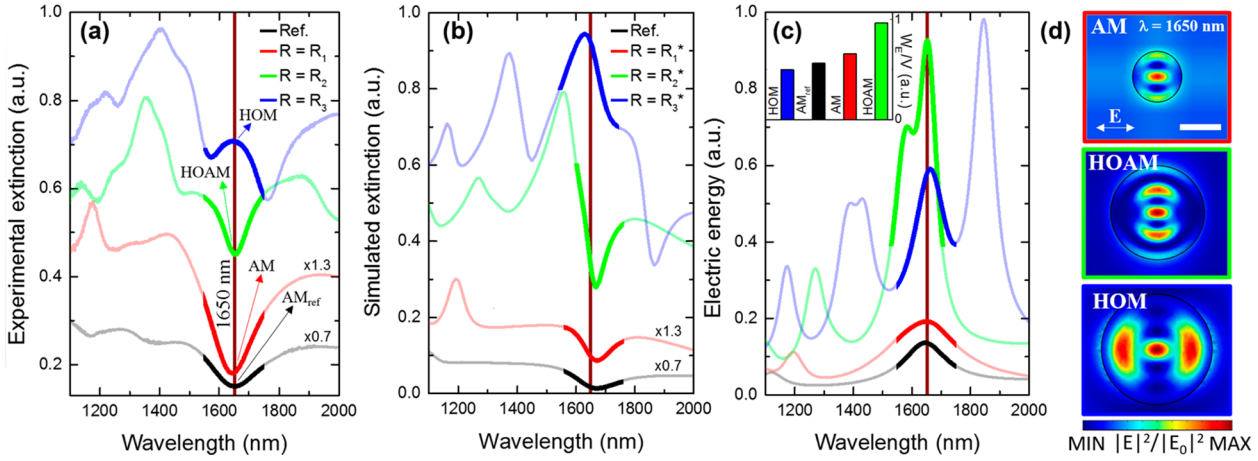

Figure 2. (a) Experimental and (b) simulated extinction spectra of nanodisks of different sizes and (c) corresponding electric energy. The inset includes values of the electric energy normalized by nanodisk volume (W_E/V) for the different resonances at 1650 nm wavelength. The experimental cross sections correspond to measured values of 1 − T (T is transmittance). The vertical lines at λ = 1650 nm refer to the incident wavelength chosen for the nonlinear experiments. (d) Simulated distribution of the electric field intensity ($|E|^2/|E_0|^2$) computed inside the nanodisk and its surroundings for the AM (top image), HOAM (middle image), and HOM (bottom image) resonances, normalized to have equal maximum intensity. Scale bar, 500 nm.

features a maximum W_E value (Figure 2c) together with a minimum extinction cross section (Figure 2a,b), describing the characteristics of the AM,[15,18] which we denote as AM_{ref} for this structure. We notice that this minimum extinction cross section has been theorized to arise from the destructive interference in the far-field between the electric dipole and toroidal dipole modes that comprise the AM.[18] Concerning the main nanodisk, whose thickness is double that of the reference one, we find that the AM occurs at a smaller radius R_1 = 350 nm < R_{ref} = 440 nm, as expected from the resonance red-shift behavior when increasing cylinder diameter or height. Surprisingly, when the radius is almost doubled from R_1 to R_2 = 635 nm, the characteristic of a dip in the extinction cross section accompanied by a maximum in the electric energy repeats at the same wavelength, indicating the presence of a higher-order anapole mode,[32] which we label as HOAM. Even though the scattering cross section at the HOAM is larger than that at the AM, when normalizing by the nanostructure surface area, both cross sections are found to deliver nearly the same value. When the radius is further increased to R_3 = 700 nm, simultaneous peaks occur in all curves due to a high-order mode (HOM) that does not have anapole characteristics. We note, from Figure 2c, that the associated value of W_E for the HOAM is 5 (7) times that for the AM (AM_{ref}), predicting the highest THG efficiency. Regarding the HOM, we find it confines less electric energy than the HOAM and more than the AM and AM_{ref}. However, as shown in the inset of Figure 2c, the HOM represents the least efficient of all modes when normalizing by nanostructure volume, while the HOAM, which exhibits the sharpest of the peaks, remains the most efficient even after the normalization.

To further describe the obtained resonances, we present their corresponding near-field intensity ($|E|^2/|E_0|^2$) distributions at 1650 nm wavelength in Figure 2d. In the top panel, the pattern corresponding to the AM is shown, exhibiting three lobes along the direction perpendicular to the incident polarization, as expected.[15,18] In the middle panel, interestingly, a similar distribution is observed for the HOAM at the center of the structure, but with two additional dim lobes at the edges of the disk arising from the higher order feature of this mode. Concerning the HOM, shown in the bottom panel, its three lobes are distributed along the direction of the excitation polarization, in contrast to both the AM and the HOAM. However, regardless of the type of mode, we observe that all three of them efficiently concentrate the electric field inside the nanodisk volume, consistent with the peaks in the electric energy, in Figure 2c.

Before presenting our THG analysis, we remark that the approach of varying the disk size at a fixed excitation wavelength (1650 nm) enables us to study the nanoantennas' nonlinear responses when excited *via* the modes of varying character, while avoiding spectral variations of germanium's intrinsic third-order nonlinear susceptibility. Certainly, even though the HOM occurs at a close wavelength of 1580 nm for the disk exhibiting the HOAM at 1650 nm ($R = R_2$, Figure 2), the associated AM appears at a distant wavelength of 2500 nm (data not shown), at which the corresponding $\chi^{(3)}$ value would differ by more than an order of magnitude.[29]

We turn now our attention toward the nonlinear characteristics of the fabricated samples, starting with the TH spectra registered from single germanium disks at the resonances of AM_{ref}, AM, HOAM, and HOM, as shown in Figure 3a. As expected from a pump wavelength of 1650 nm, a peak at 550 nm is observed for all cases, showing a trend of increasing intensity that precisely follows the order, AM_{ref} → AM → HOM → HOAM, which was predicted by our electric energy calculations (Figure 2c). Essentially, since THG is predominantly a volume phenomenon that responds mainly to the electric component of the incident wave,[13] the electric energy inside the structure at the fundamental wavelength can be used to represent the excitation power, while the observed variations in the emission, described by a third-order process, can be interpreted as a measurement of the variations in W_E^3 when the resonant mode is changed. Indeed, as shown in Figure 3b, when comparing integrated TH signals with corresponding W_E^3 values, we obtain a reasonable agreement, within a factor of ∼5, which reduces to a factor of only ∼1.3 when considering our accuracy in determining the average magnitude of the electric field ($|\bar{E}|/|E_0|$) within the dielectric, due to the high nonlinearity of the process. As it can be observed from Figure 3b, the HOAM exhibits a TH emission intensity that is between

DOI: 10.1021/acsnano.6b07568
ACS Nano 2017, 11, 953−960

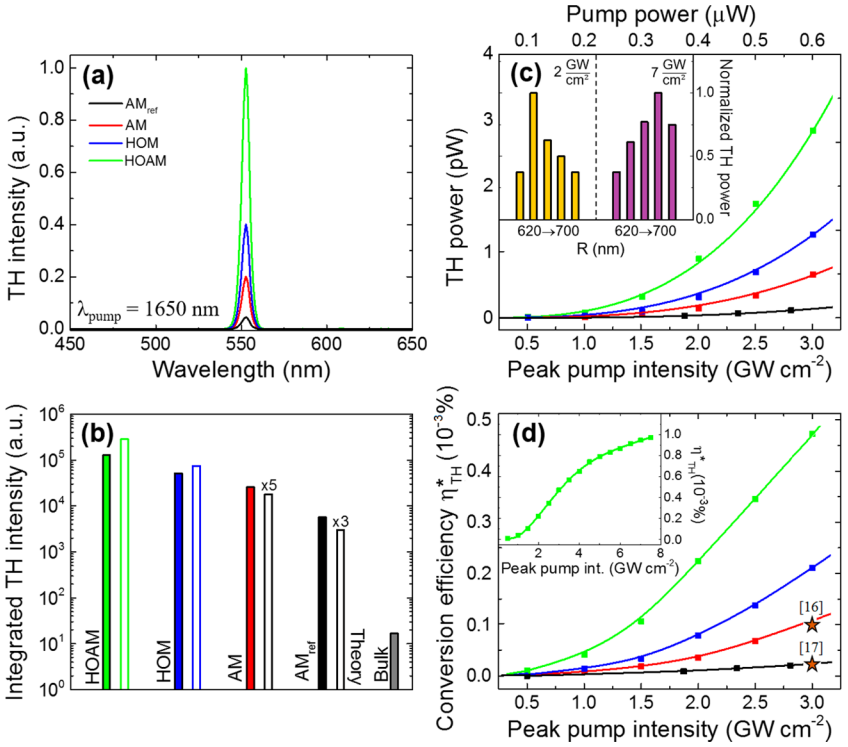

Figure 3. (a) THG spectra at the different modes excited with 1650 nm wavelength at 2 GW cm^{-2} peak pump intensity. The full width at half-maximum (fwhm) of each spectrum is ∼5 nm. (b) Measured THG performances of the studied resonances at 1650 nm fundamental wavelength. The control result from a 1.6 μm thick bulk germanium film is also included, as well as theoretical estimates (hollow bars). (c) Measured TH power *vs* peak pump intensity (with corresponding pump power in top axis) for all analyzed samples. The lines in the figure are fits considering cubic dependence of the TH power with the excitation power. The inset in the figure shows the dependence of the TH signal with the nanodisk radius for 2 GW cm^{-2} (left) and 7 GW cm^{-2} (right) peak pump intensities. Each bar represents the response of a 200 nm thick nanodisk of a different radius. (d) Conversion efficiency η_{TH}* as a function of the peak pump intensity. The added star points correspond to reported values of a silicon metasurface[16] and a quadrumer of silicon nanodisks,[17] considering a peak pump intensity of 3 GW cm^{-2}. The inset extends the characterization of the HOAM to larger excitation powers. The lines in the graph are a guide for the eyes. The peak pump intensity was estimated from the average pump power assuming 180 fs pulses at 100 kHz repetition rate.

1 and 2 orders of magnitude larger than that at the AM_{ref}, with intermediate improvements with respect to the AM and HOM cases. At the same time, this performance represents an enhancement of 4 orders of magnitude when compared to a 1.6 μm thick germanium film, whose response can be considered equivalent to that of the bulk in our experimental conditions of a tightly focused excitation beam (Rayleigh length ∼500 nm).

To analyze the dependence of the TH signal with the excitation density, we experimentally measured fundamental and harmonic powers in the range of 0−3 GW cm^{-2} peak pump intensity, as exhibited in Figure 3c for the four different resonance situations. The results show, in all cases, the expected trend of the TH intensity increasing with the cube of the pump power, as described by the third-order polynomial fits. In particular, from the fitting at the HOAM resonance, the TH conversion efficiency, defined as $\eta_{TH} = P_{peak\text{-}TH}/(P_{peak\text{-}pump})^3$ ($P_{peak\text{-}TH}$ is the peak TH power; $P_{peak\text{-}pump}$ is the peak pump power), so it does not depend on the excitation power, yields a value as high as 0.5% kW^{-2}. To the best of our knowledge, this is the highest TH conversion efficiency reported so far on the nanoscale at optical frequencies, exceeding by more than 2 orders of magnitude those of the hybrid gold/ITO nano-antenna,[25] silicon nanodisk excited at the magnetic dipole mode,[14] and thin ITO film at the epsilon-near-zero mode.[33]

An alternative definition of conversion efficiency that expresses the percentage of incident light converted into TH emission can be written as $\eta_{TH}^* = P_{peak\text{-}TH}/P_{peak\text{-}pump} = \eta_{TH} \times (P_{peak\text{-}pump})^2$, which increases quadratically with the power of the fundamental wave, as shown in Figure 3d for all studied modes. From this figure, we observe that at 3 GW cm^{-2} peak pump intensity the HOAM yields a value of η_{TH}^* of 0.0005%, which is 5 times that reported for a Fano resonant silicon metasurface[16] and more than 20 times that measured for quadrumers of silicon nanodisks supporting magnetic Fano resonance collective modes,[17] when considering the same peak pump intensity. In addition, when the incident power is further increased, the performance of our nanosystem improves even more but reaches saturation at $\eta_{TH}^* \sim 0.001\%$, as demonstrated in the inset of Figure 3d. This saturation behavior, not observed for bulk germanium, is hypothesized to arise from heating effects[34] or dense electron−hole plasma generation,[35] which alter optical characteristics of the nano-antenna, driving it off resonance, consequently causing the efficiency slope to drop.[15] Consistent with this, we find that the resonance condition shifts to larger radii when exciting above 3 GW cm^{-2} peak pump intensity, as shown in the inset of Figure 3c, where each bar corresponds to a different R value. However, additional research that could involve measuring the dependence of the extinction spectra on the pump intensity at 1650 nm, is needed to further demonstrate this point.

It is worth mentioning that in the range of excitation powers analyzed in this work, no permanent damage was produced to the samples, as no hysteresis effect as a function of pump intensity was found in any of the cases. Nonetheless,

DOI: 10.1021/acsnano.6b07568
ACS Nano 2017, 11, 953−960

irreversible changes were observed when exceeding 15 GW cm^{-2} peak pump intensity. When analyzing the origin of this damage threshold, we find that it arises not from the cumulative absorption of successive excitation pulses but from the effect of single excitation pulses. Indeed, when considering typical thermal properties for the borosilicate glass substrate,[36] characteristic thermal diffusivity lengths, calculated as $L = (\kappa \times \tau)^{1/2}$ (κ is thermal diffusivity coefficient; τ is characteristic time), reach hundreds of micrometers in the 10 μs interval between subsequent pulses, allowing efficient heat dissipation through the substrate. However, L is reduced to just <1 nm for the 180 fs intrapulse time period, giving rise to an obstacle that, without reducing the pulse duration,[37] cannot be easily addressed. In fact, we have experimentally verified that equivalent THG results are produced when using a crystalline sapphire substrate, even though it presents κ values that are more than an order of magnitude larger than those of borosilicate glass.[38] Nevertheless, we do anticipate that the TH conversion efficiency will be significantly improved if tuning the nanodisk resonance at a fundamental wavelength around 2500 nm. In this situation, a maximum in the value of $\chi^{(3)}$ and significantly lower absorption at both excitation and TH wavelengths would be attained,[29,31] reducing both heating effects and electron−hole generation due to below band gap excitation.

To deepen our analysis on the nonlinear performance of the fabricated samples, we carried out a study on the spectral tunability of the different nanoantennas. To that end, we performed measurements of the integrated TH intensity as a function of fundamental wavelength at fixed incident peak pump intensity of 2 GW cm^{-2}, as shown in Figure 4a for the reference, $R = R_1$ and $R = R_2$ nanodisks in the vicinity of 1650 nm. In order to theoretically reproduce the experimental results, in Figure 4b, we plot the cube of the calculated electric energy within the dielectric for the same spectral range, showing excellent agreement. From results in Figure 3b and Figure 4, we remark that the magnitude of the TH signal results an excellent measure of the electric energy within the dielectric, an observation we made in a previous publication based on a single case,[15] and that we now expand to modes of different character.

As it can be seen from Figure 4, the reference and $R = R_1$ nanoantennas produce two broad peaks centered at ∼1650 nm, which can be associated with the AM$_{ref}$ and AM resonances, respectively. In contrast, for the $R = R_2$ sample, two overlapping peaks are registered, which would correspond to the HOAM ($\lambda \sim$ 1650 nm) and HOM ($\lambda \sim$ 1580 nm) cases. To further analyze resonance characteristics, we performed a multipeak Gaussian fitting of both experimental and theoretical results, from which we calculated corresponding Q factor values for all four modes, as shown in the inset of Figure 4b, where a very good agreement within a factor of 1.5 is found between measurements and numerical simulations. From the inset of Figure 4b, it is observed that the Q factor doubles when switching from the AM$_{ref}$ resonance to the HOAM condition, allowing the latter to store more energy per nanometer bandwidth than the former. This key characteristic of the HOAM, which arises from the enhanced field confinement capability of this mode (Figure 2c), is the main responsible factor for the measured improved nonlinear response in Figure 3 and Figure 4.

Finally, to shed more light on the near-field intensity distributions of the analyzed modes, we acquired nonlinear images of the different nanostructures by mapping the TH emission across them using the experimental configuration described in Figure 1 (refer to the Methods section for more details of the optical setup). In Figure 5, top and middle panels, scanning electron microscopy (SEM) micrographs of 200 nm thick nanodisks and associated TH images are displayed with increasing radius from left to right, starting at $R = 350$ nm (R_1 nanodisk) and reaching up to $R = 700$ nm (R_2 nanodisk). In the bottom panel, the corresponding electric field intensity simulations at the AM, HOAM, and HOM resonances are presented. While for the smallest nanoantenna, R_1 sample, a spot of ∼500 nm fwhm is observed in its TH image, when analyzing disks with $R > 500$ nm, distinctive patterns emerge. By comparing middle and bottom panels of Figure 5 outside the diffraction-limited region, we find a remarkable resemblance with almost identical patterns for the HOAM and HOM cases, correspondingly. Indeed, since the TH light is generated exclusively where the incident electric field is accumulated, and the nanoantennas are not resonant at the TH wavelength (verified by simulations), the near-field intensity distribution at the fundamental excitation wavelength inside the nanostructure is revealed. It should be noted that the strategy adopted here is mostly susceptible to in-plane contributions of the electric field, as it probes, essentially, transverse electric radiation produced by the nanodisk.

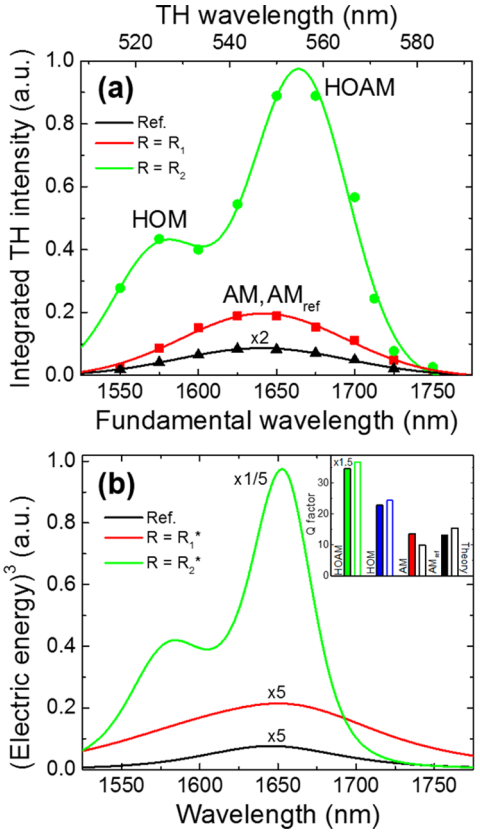

Figure 4. (a) Measured fundamental wavelength dependence of the integrated TH intensity for the $R = R_1$ and $R = R_2$ nanostructures as well as the reference nanodisk. The solid lines represent the fitting of the experimental data with Gaussian functions. (b) Corresponding spectral dependence of the simulated third power of the electric energy within the dielectric. The inset shows experimental and theoretical Q factor values corresponding to the different modes.

DOI: 10.1021/acsnano.6b07568
ACS Nano 2017, 11, 953−960

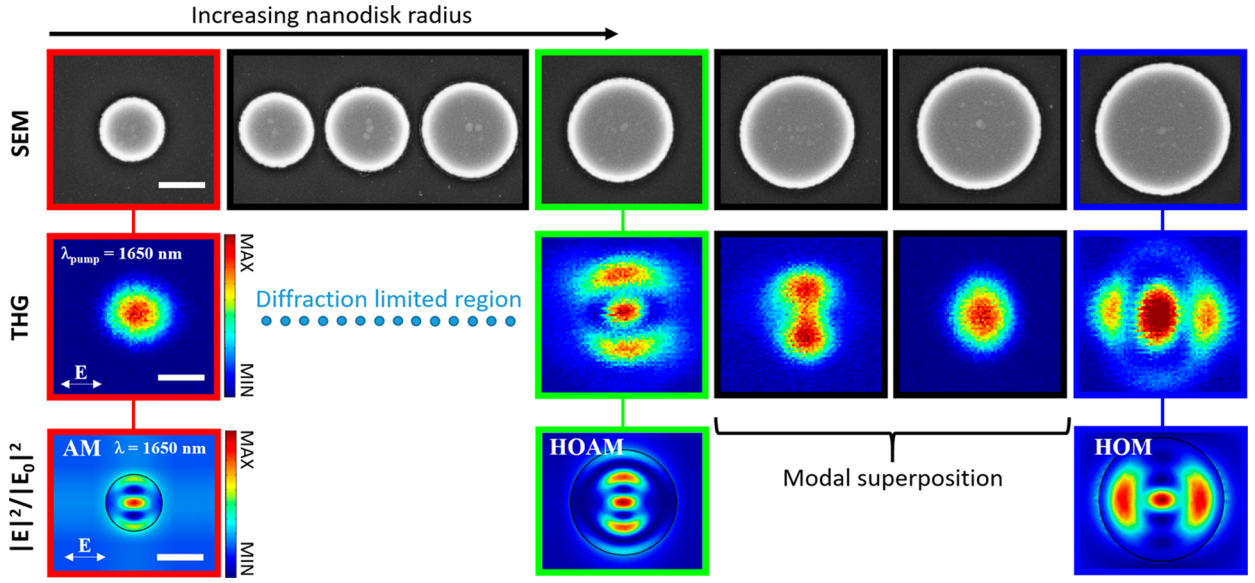

Figure 5. Top, middle, and bottom panels show, respectively, SEM micrographs, THG images, and field intensity distribution simulations of nanodisks with radius spanning from $R = R_1 = 350$ nm (left) to $R = R_3 = 700$ nm (right), with 50 nm steps. From left to right, the transition from the AM to the HOAM, and finally to the HOM, is observed. Scale bars, 500 nm.

A very high resolution of <350 nm (fwhm) can be deduced from the middle panel of Figure 5, which matches that expected for a standard optical microscope at the 550 nm TH wavelength, 0.5 × λ/NA (NA is the numerical aperture), which yields a value of 305 nm. It is worth mentioning that a similar strategy has been recently employed to image localized modes in photonic crystals through THG spatial mapping at a fundamental wavelength of 1500 nm,[39] showing <300 nm optical resolution, and registering equivalent information to that provided by complex methods such as aperture-based NSOM, which can detect electric field distributions with ∼100 nm precision.[40,41] We remark that our approach successfully probes near-field patterns with characteristic lengths of a few hundred nanometers and can be applied to a variety of modes for several different types of nanostructures, as long as they do not significantly alter the radiation pattern of the harmonic emission.

CONCLUSIONS

In conclusion, we have demonstrated that a 200 nm thick germanium nanodisk supporting the HOAM resonance produces a high TH conversion efficiency of up to 0.001% at 550 nm emission wavelength. This efficiency exceeds the nonlinear performance of bulk germanium by 4 orders of magnitude and outperforms the reported 100 nm thick germanium nanodisk at the AM_{ref}[15] and the silicon nanodisk at the magnetic dipole mode[14] by more than 1 order of magnitude and 2 orders of magnitude, respectively. In addition, we have shown that measuring the wavelength dependence of the TH signal intensity serves as an excellent method to probe relative values of the electric energy stored within the dielectric nanoantenna that is independent of the type of mode analyzed. Furthermore, through the mapping of the TH emission across the nanostructures, we have successfully imaged the near-field intensity patterns corresponding to the HOAM and HOM resonances with a high optical resolution of <350 nm, which is about one-fifth of the fundamental wavelength of 1650 nm. We find that this approach is a very useful method to characterize near-field distributions within optical nanoantennas, showing capacities equivalent to those provided by complex techniques such as NSOM in particular cases. Our findings deepen the understanding on THG processes through resonant modes in dielectric nanostructures and provide key aspects for the development of high-efficiency photon upconversion nanosystems.

METHODS

Sample Fabrication. Arrays of germanium nanodisks with 4 μm pitch and radius ranging from 300 to 700 nm were fabricated on borosilicate glass using electron beam lithography. The substrate was first coated with positive-tone PMMA (950K A4) resist and then baked for 5 min at 180 °C. The nanostructures were then defined by an electron beam exposure, followed by a development procedure.[15] Germanium thermal evaporation at 1.5 Å/s and a standard lift-off process completed the fabrication process.

Optical Characterization. Extinction measurements of the fabricated nanoantennas were performed *via* FTIR spectroscopy (Bruker Hyperion 2000) using unpolarized light at normal incidence in transmission mode, averaging over arrays of 20 × 20 disks for each diameter value. For the nonlinear characterization of individual nanostructures, THG studies were carried out with the experimental setup sketched in Figure 1. A pulsed Yb:KGW PHAROS laser system was used as the pump of a collinear optical parametric amplifier ORPHEUS with a LYRA wavelength extension option (Light Conversion Ltd., pulse duration of 180 fs, repetition rate of 100 kHz). The excitation beam (λ = 1500−1800 nm) was reflected by a short-pass dichroic mirror (Thorlabs DMSP1000) and focused onto the sample with a 100× (NA = 0.9) air objective from Nikon. The TH emission was collected in a backscattering configuration *via* the same objective and detected with an avalanche photodiode (MPD PDM series by Picoquant) for imaging or by a spectrograph (PI Acton SP2300 by Princeton Instruments) for spectral measurements. The sample was fixed to an *XYZ* piezo-scanner stage (Nano-Drive, Mad City Laboratories) to perform the scanning. The conversion efficiency was determined by directly measuring the collected TH emission power with a calibrated silicon photodetector (Newport), and the excitation power with a germanium photodetector (Thorlabs), and then computing the ratio between the both. For <1 pW TH powers, values were calibrated by using the measured TH spectra. Finally,

DOI: 10.1021/acsnano.6b07568
ACS Nano 2017, 11, 953−960

efficiency values were corrected by the factor (collection surface area)/(surface area emitting TH light), as deduced from nonlinear images.

Numerical Simulations. Theoretical calculations of the extinction cross-section spectra and the near-field intensity distributions were performed using the RF module of the commercial software Comsol Multiphysics. Simulations were carried out within a 4 μm diameter sphere containing the germanium nanodisk on a glass substrate and surrounded by air medium. The problem was solved for the scattered field using scattering boundary conditions and a perfectly matched layer of 50 nm thickness. The extinction cross section was calculated as the sum of the absorption and scattering cross sections, that is, $\sigma_{ext} = \sigma_{abs} + \sigma_{scatt}$, considering linearly polarized light at normal incidence. The absorption cross section was computed over the nanodisk volume, while the scattering cross section was calculated as the field scattered over a semisphere placed opposite to the direction of incidence of the pump wave. Simulations of the electric energy stored inside the nanostructure were performed by integrating the electric field intensity within the nanodisk using the expression $W_E = n^2 \int\int\int |E|^2 dV/2$. We note that by considering the formula for the dispersive medium,[42] $W_E = \frac{\partial(\varepsilon_r \omega)}{\partial \omega} \iiint |E|^2 dV/2$ (ε_r is the relative permittivity), only minor differences arise due to the nearly constant value of ε_r for germanium in the spectral range of interest.[31]

AUTHOR INFORMATION

Corresponding Authors

*E-mail: g.grinblat@imperial.ac.uk.

*E-mail: yi.li@imperial.ac.uk.

ORCID

Gustavo Grinblat: 0000-0002-1637-9524

Author Contributions

G.G. and Y.L. contributed equally to this work.

Notes

The authors declare no competing financial interest.

ACKNOWLEDGMENTS

The authors acknowledge funding provided by the EPSRC Reactive Plasmonics Programme (EP/M013812/1), the EPSRC Mathematical Fundamentals of Metamaterials Programme (EP/L024926/1), ONR Global, the Royal Society, and the Lee-Lucas Chair in Physics. Requests for data should be sent to datainquiryEXSS@imperial.ac.uk.

REFERENCES

(1) Li, R.; Ji, Z.; Dong, J.; Chang, C. H.; Wang, X.; Sun, B.; Wang, M.; Liao, Y. P.; Zink, J. I.; Nel, A. E.; Xia, T. Enhancing the Imaging and Biosafety of Upconversion Nanoparticles through Phosphonate Coating. *ACS Nano* **2015**, *9*, 3293−3306.

(2) Weigelin, B.; Bakker, G. J.; Friedl, P. Third Harmonic Generation Microscopy of Cells and Tissue Organization. *J. Cell Sci.* **2016**, *129*, 245−255.

(3) Arppe, R.; Näreoja, T.; Nylund, S.; Mattsson, L.; Koho, S.; Rosenholm, J. M.; Soukka, T.; Schäferling, M. Photon Upconversion Sensitized Nanoprobes for Sensing and Imaging of pH. *Nanoscale* **2014**, *6*, 6837−6843.

(4) Alonso-Cristobal, P.; Vilela, p; El-Sagheer, A.; Lopez-Cabarcos, E.; Brown, T.; Muskens, O. L.; Rubio-Retama, J.; Kanaras, A. G. Highly Sensitive DNA Sensor Based on Upconversion Nanoparticles and Graphene Oxide. *ACS Appl. Mater. Interfaces* **2015**, *7*, 12422−12429.

(5) van Sark, W. G. J. H. M.; de Wild, J.; Rath, J. K.; Meijerink, A.; Schropp, R. E. I. Upconversion in Solar Cells. *Nanoscale Res. Lett.* **2013**, *8*, 81.

(6) Ogawa, T.; Yanai, N.; Monguzzi, A.; Kimizuka, N. Highly Efficient Photon Upconversion in Self-Assembled Light-Harvesting Molecular Systems. *Sci. Rep.* **2015**, *5*, 10882.

(7) Wang, C.; Cheng, L.; Liu, Z. Drug Delivery with Upconversion Nanoparticles for Multi-functional Targeted Cancer Cell Imaging and Therapy. *Biomaterials* **2011**, *32*, 1110−1120.

(8) Li, K.; Su, Q.; Yuan, W.; Tian, B.; Shen, B.; Li, Y.; Feng, W.; Li, F. Ratiometric Monitoring of Intracellular Drug Release by an Upconversion Drug Delivery Nanosystem. *ACS Appl. Mater. Interfaces* **2015**, *7*, 12278−12286.

(9) Efimov, A.; Taylor, A. J.; Omenetto, F. G.; Knight, J. C.; Wadsworth, W. J.; Russell, P. S. J. Phase-Matched Third Harmonic Generation in Microstructured Fibers. *Opt. Express* **2003**, *11*, 2567−2576.

(10) Sasagawa, K.; Tsuchiya, M. Highly Efficient Third Harmonic Generation in a Periodically Poled MgO:$LiNbO_3$ Disk Resonator. *Appl. Phys. Express* **2009**, *2*, 122401.

(11) Miyata, K.; Petrov, V.; Noack, F. High-Efficiency Single-Crystal Third-Harmonic Generation in BiB_3O_6. *Opt. Lett.* **2011**, *36*, 3627−3629.

(12) Liu, M.; Quah, H. S.; Wen, S.; Yu, Z.; Vittal, J. J.; Ji, W. Efficient Third Harmonic Generation in a Metal−Organic Framework. *Chem. Mater.* **2016**, *28*, 3385−3390.

(13) Boyd, R. W. *Nonlinear Optics*; Academic Press, 2008.

(14) Shcherbakov, M. R.; Neshev, D. N.; Hopkins, B.; Shorokhov, A. S.; Staude, I.; Melik-Gaykazyan, E. V.; Decker, M.; Ezhov, A. A.; Miroshnichenko, A. E.; Brener, I.; Fedyanin, A. A.; Kivshar, Y. S. Kivshar. Enhanced Third-Harmonic Generation in Silicon Nanoparticles Driven by Magnetic Response. *Nano Lett.* **2014**, *14*, 6488−6492.

(15) Grinblat, G.; Li, Y.; Nielsen, M.; Oulton, R. F.; Maier, S. A. Enhanced Third Harmonic Generation in Single Germanium Nanodisks Excited at the Anapole Mode. *Nano Lett.* **2016**, *16*, 4635−4640.

(16) Yang, Y.; Wang, W.; Boulesbaa, A.; Kravchenko, I. I.; Briggs, D. P.; Puretzky, A.; Geohegan, D.; Valentine, J. Nonlinear Fano-Resonant Dielectric Metasurfaces. *Nano Lett.* **2015**, *15*, 7388−7393.

(17) Shorokhov, A. S.; Melik-Gaykazyan, E. V.; Smirnova, D. A.; Hopkins, B.; Chong, K. E.; Choi, D. Y.; Shcherbakov, M. R.; Miroshnichenko, A. E.; Neshev, D. N.; Fedyanin, A. A.; Kivshar, Y. S. Multifold Enhancement of Third-Harmonic Generation in Dielectric Nanoparticles Driven by Magnetic Fano Resonances. *Nano Lett.* **2016**, *16*, 4857−4861.

(18) Miroshnichenko, A. E.; Evlyukhin, A. B.; Yu, Y. F.; Bakker, R. M.; Chipouline, A.; Kuznetsov, A. I.; Luk'yanchuk, B.; Chichkov, B. N.; Kivshar, Y. S. Nonradiating Anapole Modes in Dielectric Nanoparticles. *Nat. Commun.* **2015**, *6*, 8069.

(19) Caldarola, M.; Albella, P.; Cortés, E.; Rahmani, M.; Roschuk, T.; Grinblat, G.; Oulton, R. F.; Bragas, A. V.; Maier, S. A. Non-Plasmonic Nanoantennas for Surface Enhanced Spectroscopies with Ultra-Low Heat Conversion. *Nat. Commun.* **2015**, *6*, 7915.

(20) Bakker, R. M.; Permyakov, D.; Yu, Y. F.; Markovich, D.; Paniagua-Domínguez, R.; Gonzaga, L.; Samusev, A.; Kivshar, Y.; Luk'yanchuk, B.; Kuznetsov, A. I. Magnetic and Electric Hotspots with Silicon Nanodimers. *Nano Lett.* **2015**, *15*, 2137−2142.

(21) Halas, N. J.; Lal, S.; Chang, W.-S.; Link, S.; Nordlander, P. Plasmons in Strongly Coupled Metallic Nanostructures. *Chem. Rev.* **2011**, *111*, 3913−3961.

(22) Giannini, V.; Fernández-Domínguez, A. I.; Heck, S. C.; Maier, S. A. Plasmonic Nanoantennas: Fundamentals and their Use in Controlling the Radiative Properties of Nanoemitters. *Chem. Rev.* **2011**, *111*, 3888−3912.

(23) Lippitz, M.; van Dijk, M. A.; Orrit, M. Third-Harmonic Generation from Single Gold Nanoparticles. *Nano Lett.* **2005**, *5*, 799−802.

(24) Metzger, B.; Hentschel, M.; Schumacher, T.; Lippitz, M.; Ye, X.; Murray, C. B.; Knabe, B.; Buse, K.; Giessen, H. Doubling the Efficiency of Third Harmonic Generation by Positioning ITO Nanocrystals into the Hot-Spot of Plasmonic Gap-Antennas. *Nano Lett.* **2014**, *14*, 2867−2872.

(25) Aouani, H.; Rahmani, M.; Navarro-Cía, M.; Maier, S. A. Third-Harmonic-Upconversion Enhancement from a Single Semiconductor

DOI: 10.1021/acsnano.6b07568
ACS Nano 2017, 11, 953−960

Nanoparticle Coupled to a Plasmonic Antenna. *Nat. Nanotechnol.* **2014**, *9*, 290−294.
(26) Das, S. K.; Güell, F.; Gray, C.; Das, P. K.; Grunwald, R.; McGlynn, E. ZnO Nanorods for Efficient Third Harmonic UV Generation. *Opt. Mater. Express* **2014**, *4*, 701−709.
(27) Hajisalem, G.; Hore, D. K.; Gordon, R. Interband Transition Enhanced Third Harmonic Generation from Nanoplasmonic Gold. *Opt. Mater. Express* **2015**, *5*, 2217−2224.
(28) Metzger, B.; Schumacher, T.; Hentschel, M.; Lippitz, M.; Giessen, H. Third Harmonic Mechanism in Complex Plasmonic Fano Structures. *ACS Photonics* **2014**, *1*, 471−476.
(29) Zhang, L.; Agarwal, A. M.; Kimerling, L. C.; Michel, J. Nonlinear Group IV Photonics Based on Silicon and Germanium: from Near-Infrared to Mid-Infrared. *Nanophotonics* **2014**, *3*, 247−268.
(30) Rakić, A. D.; Djurišic, A. B.; Elazar, J. M.; Majewski, M. L. Optical Properties of Metallic Films for Vertical-Cavity Optoelectronic Devices. *Appl. Opt.* **1998**, *37*, 5271−5283.
(31) Palik, E. D. *Handbook of Optical Constants of Solids*; Academic Press, 1998.
(32) Zhai, W. C.; Qiao, T. Z.; Cai, D. J.; Wang, W. J.; Chen, J. D.; Chen, Z. H.; Liu, S. D. Anticrossing Double Fano Resonances Generated in Metallic/Dielectric Hybrid Nanostructures using Non-radiative Anapole Modes for Enhanced Nonlinear Optical Effects. *Opt. Express* **2016**, *24*, 27858−27869.
(33) Luk, T. S.; De Ceglia, D.; Liu, S.; Keeler, G. A.; Prasankumar, R. P.; Vincenti, M. A.; Scalora, M.; Sinclair, M. B.; Campione, S. Enhanced Third Harmonic Generation from the Epsilon-Near-Zero Modes of Ultrathin Films. *Appl. Phys. Lett.* **2015**, *106*, 151103.
(34) Yeshchenko, O. A.; Bondarchuk, I. S.; Gurin, V. S.; Dmitruk, I. M.; Kotko, A. V. Temperature Dependence of the Surface Plasmon Resonance in Gold Nanoparticles. *Surf. Sci.* **2013**, *608*, 275−281.
(35) Makarov, S.; Kudryashov, S.; Mukhin, I.; Mozharov, A.; Milichko, V.; Krasnok, A.; Belov, P. Tuning of Magnetic Optical Response in a Dielectric Nanoparticle by Ultrafast Photoexcitation of Dense Electron−Hole Plasma. *Nano Lett.* **2015**, *15*, 6187−6192.
(36) Ghosh, S.; Ghosh, A.; Mukherjee, J.; Banerjee, R. Improved Thermal Properties of Borosilicate Glass Composite Containing Single Walled Carbon Nanotube Bundles. *RSC Adv.* **2015**, *5*, 51116−51121.
(37) Smith, A. V.; Do, B. T.; Hadley, G. R.; Farrow, R. L. Optical Damage Limits to Pulse Energy From Fibers. *IEEE J. Sel. Top. Quantum Electron.* **2009**, *15*, 153−158.
(38) Morikawa, J.; Orie, A.; Hashimoto, T.; Juodkazis, S. Thermal and Optical Properties of the Femtosecond-Laser-Structured and Stress-Induced Birefringent Regions in Sapphire. *Opt. Express* **2010**, *18*, 8300−8310.
(39) Moerland, R.; van Hulst, N.; Gersen, H.; Kuipers, L. Probing the Negative Permittivity Perfect Lens at Optical Frequencies using Near-Field Optics and Single Molecule Detection. *Opt. Express* **2005**, *13*, 1604−1614.
(40) Fleischer, M. Near-Field Scanning Optical Microscopy Nanoprobes. *Nanotechnol. Rev.* **2012**, *1*, 313−338.
(41) Zeng, Y.; Roland, I.; Checoury, X.; Han, Z.; El Kurdi, M.; Sauvage, S.; Gayral, B.; Brimont, C.; Guillet, T.; Semond, F.; Boucaud, P. Imaging of Photonic Crystal Localized Modes through Third-Harmonic Generation. *ACS Photonics* **2016**, *3*, 1240−1247.
(42) Landau, L. D.; Lifshitz, E. M. *Electrodynamics of Continuous Media*; Pergamon Press, 1960.

DOI: 10.1021/acsnano.6b07568
ACS Nano 2017, 11, 953−960